Breaking the ice: Identifying hydraulically-forced crevassing

Thomas Samuel Hudson[1], Alex Mark Brisbourne[2], Robert Stephen White[3], John-Michael Kendall[1], Robert J. Arthern[4], and Andrew Mark Smith[2]

[1]University of Oxford
[2]British Antarctic Survey
[3]Bullard Laboratories
[4]British Antarctic Survey, Natural Environment Research Council

November 23, 2022

Abstract

Hydraulically-forced crevassing is thought to reduce the stability of ice shelves and ice sheets, affecting structural integrity and providing pathways for surface meltwater to the bed. It can cause ice shelves to collapse and ice sheets to accelerate into the ocean. However, direct observations of the hydraulically-forced crevassing process remain elusive. Here we report a new, novel method and observations that use icequakes to directly observe crevassing and determine the role of hydrofracture. Crevasse icequake depths from seismic observations are compared to a theoretically derived maximum-dry-crevasse-depth. We observe icequakes below this depth, suggesting hydrofracture. Furthermore, icequake source mechanisms provide insight into the fracture process, with predominantly opening cracks observed, which have opening volumes of tens to hundreds of cubic meters. Our method and findings provide a framework for studying a critical process, key for the stability of ice shelves and ice sheets, and hence rates of future sea-level rise.

Breaking the ice: Identifying hydraulically-forced crevassing

T.S. Hudson[1*], A.M. Brisbourne[2], R.S. White[3], JM. Kendall[1], R. Arthern[2], A.M. Smith[2]

[1] *Department of Earth Sciences, University of Oxford, Oxford, UK*

[2] *British Antarctic Survey, Cambridge, UK*

[3] *Bullard Laboratories, University of Cambridge, Cambridge, UK*

Corresponding author: Thomas S. Hudson (thomas.hudson@earth.ox.ac.uk)

Key Points:

- We demonstrate a novel method for using crevasse icequake depths to discriminate between dry and hydrofracture driven surface crevassing
- Icequakes can be used to directly observe and elucidate the crevasse hydrofracture process
- Icequakes show tensile crack failure with opening volumes calculated from moment magnitudes

Abstract

Hydraulically-forced crevassing is thought to reduce the stability of ice shelves and ice sheets, affecting structural integrity and providing pathways for surface meltwater to the bed. It can cause ice shelves to collapse and ice sheets to accelerate into the ocean. However, direct observations of the hydraulically-forced crevassing process remain elusive. Here we report a new, novel method and observations that use icequakes to directly observe crevassing and determine the role of hydrofracture. Crevasse icequake depths from seismic observations are compared to a theoretically derived maximum-dry-crevasse-depth. We observe icequakes below this depth, suggesting hydrofracture. Furthermore, icequake source mechanisms provide insight into the fracture process, with predominantly opening cracks observed, which have opening volumes of tens to hundreds of cubic meters. Our method and findings provide a framework for studying a critical process, key for the stability of ice shelves and ice sheets, and hence rates of future sea-level rise.

1 Introduction

Hydraulically-forced surface crevassing, also referred to as hydrofracture, has the potential to significantly influence the stability of glaciers, ice sheets and ice shelves (Lai et al., 2020). On glaciers and ice sheets, hydraulically-forced crevassing provides a potential pathway for surface meltwater to reach and lubricate the bed (Das et al., 2008; Van Der Veen, 1998; Weertman, 1973), enhancing basal sliding of ice into the ocean (Rignot & Kanagaratnam, 2006), accelerating sea-level rise. Hydraulically-forced surface crevassing on ice shelves can result in catastrophic failure, with melt ponds promoting fracture that can lead to the collapse of the ice shelf (Hughes, 1983; Mcgrath et al., 2012; T. Scambos et al., 2003; T. A. Scambos et al., 2000). Following ice shelf collapse, land-based glaciers can accelerate into the ocean, since the buttressing provided by the ice shelf no longer exists, again contributing to sea-level rise. Understanding the fundamental mechanism of hydraulically-forced surface crevassing is therefore a particularly timely topic within glaciology.

Here, we present icequake observations from Skeidararjökull, an outlet glacier of the Vatnajökull Ice Cap, Iceland. This glacier is an ideal environment for studying potential hydraulically-forced crevassing due to the high levels of surface melt present. Previous studies have used icequakes to infer hydraulically-forced crevassing using auxiliary information, such as glacier speed up (Helmstetter et al., 2015), or the presence of meltwater (Carmichael et al., 2012, 2015). Others have used seismicity to show that crevassing exhibits tensile faulting (Mikesell et al., 2012; Neave & Savage, 1970; Roux et al., 2010; Walter et al., 2009). We first present a novel method for attributing an icequake to either dry or hydraulically-forced crevassing, providing evidence that the icequakes we observe are likely induced by hydrofracture. We then use icequake source mechanisms to confirm the crevassing stress release mechanism. Our results provide for the first time direct evidence of hydrofracture, offering insights into this previously elusive process.

2 Methods

Here, we briefly describe the methods for detecting and locating the seismicity, as well as an overview of how the source mechanism inversions are undertaken and moment magnitudes, M_w, are calculated. Two additional fundamental methods used in this study are obtaining crevasse icequake depths from P-to-Rayleigh-wave amplitude ratios and the calculation of a theoretical maximum-dry-crevasse-depth, based on the rheology of ice. These methods and theory are too complex to adequately describe in the main text, so we instead describe them in the Supplementary Information (Supplementary Text S1 and S2, respectively).

2.1 Seismicity

The seismicity presented in this study is detected using QuakeMigrate (Hudson et al., 2019; Smith et al., 2020), with the method and overall catalogue of icequakes detailed by Hudson et al (2019). We relocate the detected earthquakes using NonLinLoc (Lomax & Virieux, 2000) to obtain more accurate epicentral locations. For the subset of events presented in detail in Figure 1 and 2, we manually pick P and S phase arrivals before relocation. The crevassing icequake hypocentral depths for the selected events are obtained using P-to-Rayleigh-wave amplitude ratios, with the associated method details given in the Supplementary Information (Supplementary Text S1).

The icequake source mechanisms are obtained by performing a Bayesian full waveform source inversion using an identical approach to a method detailed by Hudson et al (n.d.). Only P-wave phases are used since the horizontal components are generally too noisy to use, due to the instruments melting out of the glacier. Theoretically, S and surface waves could also be used to constrain the inversion, but the amplitudes of any S arrivals are generally close to the noise levels and we have low confidence in our ability to model the polarity of dispersive surface waves sufficiently accurately for a moment tensor inversion, given the depth dependent velocity structure of the firn layer at the site. We use a finite difference scheme to model the Green's functions used to produce the synthetic seismograms in the inversion. The depth of the source, a critical parameter affecting the source inversion, is constrained using P-to-Rayleigh amplitude ratios.

The moment magnitude, M_w, of the icequakes is calculated using a spectral method(Stork et al., 2014). The spectrum of the icequake is calculated by performing multi-taper spectral estimation(Krischer, 2016; Prieto et al., 2009) in order to find the long period spectral level and hence the seismic moment release, M_0. M_w can then be calculated from (Hanks & Kanamori, 1979),

$$M_w = \frac{2}{3}\log_{10}(M_0) - 6.0. \qquad (1)$$

If one assumes that all the moment release for a given icequake is released via tensile failure, then the opening of a crack, ΔV, can be calculated from,

$$\Delta V = \frac{M_0}{\sigma_T} \qquad (2)$$

where σ_T is the tensile strength of the ice, taken to be 1.5 MPa (Podolskiy & Walter, 2016) in this study.

3 Results

3.1 Evidence for dry fracture vs. hydrofracture from crevasse depth

As a crevasse propagates, the ice fractures, releasing seismic energy as icequakes. Crevasses ordinarily only propagate to a certain depth within the ice column, where the tensile stress field causing crevasse opening is compensated by the ice overburden pressure acting to close the crevasse. We refer to this depth limit as the maximum-dry-crevasse-depth, d^*. However, if the crevasse contains sufficient water, the additional pressure of this water column can overcome the ice overburden pressure and induce hydrofracture, allowing the crevasse to propagate to greater depths (Nick et al., 2010; Van Der Veen, 1998). Therefore, if the observed depth of a crevasse icequake is greater than d^*, then one can infer that the icequake is induced by hydrofracture. This is the fundamental premise of this study.

However, obtaining sufficiently accurate icequake hypocentral depths for comparison to d^* is non-trivial. Seismometer networks are inherently poor at constraining the depth of an earthquake using traditional body wave methods if the source-receiver epicentral distance is much greater than the source depth. This is generally the case in our study. Since the depth of an icequake is critical evidence for or against hydrofracture, a more accurate method is required for constraining hypocentral depth. We use surface-wave information in the form of P-wave to Rayleigh-wave amplitude ratios to constrain hypocentral depth (Heyburn et al., 2013; Jia et al., 2017; Stein & Wiens, 1986; Tsai & Aki, 1970). Figure 1a shows finite-difference full-waveform modelling results (Larsen et al., 2001) and observations of P to Rayleigh amplitude ratios, plotted against epicentral distance for a range of crevasse depths. The observed amplitude ratios are compared to the model results to calculate the crevassing depths. We independently verify these crevasse depths using P-S delay-times from receivers close to the source epicentre where possible (See Supplementary Figure S1), giving us confidence that the amplitude ratios provide a sufficiently accurate estimation of icequake depth.

The crevassing depths constrained by the observations in Figure 1 can then be compared to the maximum-dry-crevasse-depths, shown in Figure 2b, derived from the surface velocity field shown in Figure 2a. Figure 2c shows the epicentral locations of the near surface seismicity, with the grey scatter points showing the automatically detected icequakes(Thomas S Hudson et al., 2019) and the coloured scatter points showing a subset of manually relocated events. The majority of this subset of icequakes are located below d^* (solid red line, Figure 2d), on average 7.4 m deeper, from which we infer that they may be induced by hydrofracture.

One potential limitation of using the source depth to discriminate between hydrofracture and dry fracture is that we do not account for dynamic rupture, whereby during the rupture, a crack may propagate deeper than the prevailing stress field otherwise allows, initiated by fracture tip instability (Buehler & Gao, 2006). For the purposes of this study we treat each icequake as an instantaneous point source, therefore neglecting dynamic rupture. Although this assumption is does not fully describe the physics of the source, we deem it appropriate here because of the distinct, high-frequency and short-duration phase arrivals observed.

Given that the events are predominantly deeper than d^*, we suggest that the majority of these events are likely caused by hydraulically-forced crevassing. In any case, the methodologies developed here, which constrain icequake depth from amplitude ratios and use this source depth to discriminate hydrofracture, are important developments for studying hydrofracture-induced crevassing.

3.2 Crevassing source mechanisms

Moment tensor inversions constrain whether icequake source mechanisms include explosive, implosive, crack, or shear components. Icequake magnitudes then give the volume of opening, or fault area and displacement, depending upon the icequake source mechanism.

Figure 2c shows the P-wave-constrained moment tensor inversion results for the subset of icequakes for which sufficiently accurate depths have been obtained. The inversion results for two of these icequakes are presented in more detail in Figure 3. For both icequakes, the waveform polarities are all correctly inverted for. Lune plots (Tape & Tape, 2012) in Figure 3b and Figure 3d indicate that the most likely source mechanisms for the two icequakes are a closing and an opening crack, respectively, with a negligible shear component in both cases. Such crack mechanisms are the mode of failure one might expect from either dry or hydraulically-forced crevassing. However, after considering the Probability Density Function (PDF) of the inversion solutions for the closing crack icequake in Figure 3b, an opening crack mechanism cannot be eliminated. This ambiguity is due to station geometry on the focal sphere. In any case, an opening or closing crack of a specific orientation is required to represent the observations adequately, as inferred from previous seismic observations (Mikesell et al., 2012; Neave & Savage, 1970; Roux et al., 2010; Walter et al., 2009).

All icequake crack orientations in Figure 2c agree with the principal stress directions calculated from the observed surface velocities, as shown by the orange vectors in Figure 2c. This confirms interpretations in previous studies (Garcia et al., 2019; Harper et al., 1998). The apparent closing crack observation for the icequake at 64.327° N, 17.21° W may be supported by the presence of tensile stresses in both principal stress directions. In such a stress regime, a closing crack may be valid, effectively exhibiting two-dimensional necking in the surface-parallel plane.

The moment magnitude of the crevassing icequakes range from -0.4 to -0.9, calculated using a spectral method (Stork et al., 2014). If we approximate all the failure as tensile, then for a tensile strength of ice of 1.5 MPa (Podolskiy & Walter, 2016), the volume associated with crack opening or closing is of the order of $30\ m^3$ to $150\ m^3$.

We propose several possible mechanisms for generating seismicity below the maximum-dry-crevasse-depth. These interpretations are summarised in Figure 4. The mechanisms are: (1) new cracks opening when the combined deviatoric near-surface stress field and hydrostatic pressure are sufficient to overcome the ice overburden pressure and tensile strength of the ice; (2) pre-existing cracks that have closed reopening due to a sufficient head of water in the crevasse; (3) opened pre-existing cracks reclosing as the water is evacuated from the fracture, due to a preferential pressure gradient below the fracture.

For mechanisms 2 and 3, the crevasse must have propagated to that depth via mechanism 1, therefore suggesting that at least some of the icequakes we observe are likely to be new ice fracture. We observe principal tensile stress amplitudes of greater than 200 kPa (see Figure S2), more than sufficient to overcome an ice tensile strength of ~100 kPa (Paterson, 1994). Mechanism 2 is similar to mechanism 1, except requiring a lower hydrostatic pressure to induce crack opening, and is possible if crevasses have formed upstream and subsequently been closed by principal compressive stresses perpendicular to the crevasse. Such refracturing is proposed in scenarios where there are insufficient volumes of surface meltwater to immediately establish a permanent bed connection (Boon & Sharp, 2003). Mechanism 3 is presented more tentatively, partly due to the potential ambiguity of the closing-crack source mechanism (see Figure 3a), but also because these crevasses would have to close over sufficiently short time scales to generate the ~100 Hz source frequencies observed in the P-wave spectra. While ice can suddenly fail or reopen a crack over such a short duration, a possible source of driving stresses or pressures required to close cracks this quickly is less conceivable. A crack at greater depth could reopen, evacuating water from above, but envisaging a sufficiently localised stress field is difficult. Alternatively, water may travel through an opening, pre-existing crack sufficiently quickly that the crack then immediately closes, although the magnitude of closing would have to dominate over opening to explain a closing-crack observation. In summary, we therefore confidently present mechanisms 1 and 2, but suggest that mechanism 3 is unlikely.

One question that arises is why we do not observe seismicity via mechanism 1 or 2 occurring all the way to the glacier bed, as is proposed in various studies (Boon & Sharp, 2003; Carmichael et al., 2012; Colgan et al., 2016; Van Der Veen, 1998; Weertman, 1973). A reason could be that as such fractures penetrate deeper into the glacier, the energy will be more attenuated, fall below background noise levels and not be detected. Alternatively, the crevasses at Skeidararjökull might never reach the bed.

These results emphasise the potential information that icequakes hold for elucidating the physics of glacier hydrofracture. Here, we only use P-waves to constrain the mechanisms, but if one had a more comprehensive dataset with a greater number of receivers and higher SNR, then it may be possible to constrain the source mechanism better. Furthermore, if one were to invert for a dynamic rupture model of finite length, rather than the instantaneous point source that we assume here, then one might gain additional insight into the physics governing hydrofracture in ice. Another approach to learn more about the hydrofracture process could be to compare observations such as ours to theoretical models of crevasse vibrational modes to infer crevasse geometry (Lipovsky & Dunham, 2015), or even models of supraglacial lake drainage (Jones et al., 2013).

4 Implications for ice sheet and ice shelf stability

Our findings provide a method for observing hydrofracture at icesheets such as the Greenland Ice Sheet, where although it has been shown that meltwater can drain from the surface to the bed (Das et al., 2008), the mechanism and pathway has not been imaged previously. Calving at the ocean termini of outlet glaciers of the Greenland Ice Sheet could also be enhanced by hydrofracture. Increased calving could be facilitated by precipitation increasing the hydrostatic pressure of water-filled crevasses (O'Neel et al., 2003), or by damage to the upstream ice (Krug et al., 2014), with the depth of this damage through the ice column dependent upon the depth of the crevasses, which we infer here to be controlled by the glacier stress state and hydrofracture. Our method could provide observations of the depth of such damage. The above mechanisms are also hypothesised to be important factors that could accelerate the collapse of the West Antarctic Ice Sheet and cause significant retreat of the East Antarctic Ice Sheet (Pollard et al., 2015).

Some ice shelves exhibit surface melt ponds before undergoing disintegration, whereas others have similar melt ponds but remain intact (Scambos et al., 2000). Crevassing icequakes could provide insight into whether hydrofracture is occurring unnoticed at these apparently stable ice shelves, potentially leading to sudden future catastrophic collapse, or whether hydrofracture is physically suppressed by another mechanism that affects either the stress regime or the fracture toughness of the ice.

In conclusion, understanding the stability of ice sheets and ice shelves is important for sea-level-rise projections (Vaughan et al., 2013). Hydrofracture induced crevassing is an important mechanism that, at least to some extent, controls the stability of such ice bodies.

The methodology and findings we present provide a means of attributing crevassing icequakes to hydrofracture. We show that such icequakes can then be used as an observational basis for studying the physical mechanisms associated with hydrofracture induced crevassing.

Acknowledgements

T. Hudson was funded by a Natural Environment Research Council (NERC) Studentship (NE/L002507/1) for the majority of this work. We thank Antony Butcher for useful conversations regarding the waveform propagation modelling. We thank Hunter Philson, University of Iceland and the Icelandic Glaciological Society for fieldwork support, without which this study would not have been possible. We also thank Finnur Pálsson and the glaciology group at the University of Iceland for the radar bed topography data, and Robert Green for pre-processing the data. Seismometers were borrowed from SeisUK (Geophysical Equipment Facility loan number 1022) and NERC British Antarctic Survey. Seismic data will be made available on IRIS. Software used includes: QuakeMigrate (https://github.com/QuakeMigrate); NonLinLoc (http://alomax.free.fr/nlloc/); SeisSrcInv (https://github.com/TomSHudson/SeisSrcInv) for the moment tensor inversion; SeisSrcMoment (https://github.com/TomSHudson/SeisSrcMoment) for the moment magnitude calculation.

References

Björnsson, H. (2017). *The Glaciers of Iceland*. Paris: Atlantis Press. https://doi.org/10.2991/978-94-6239-207-6

Boon, S., & Sharp, M. (2003). The role of hydrologically-driven ice fracture in drainage system evolution on an Arctic glacier. *Geophysical Research Letters*, *30*(18), 3–6. https://doi.org/10.1029/2003GL018034

Buehler, M. J., & Gao, H. (2006). Dynamical fracture instabilities due to local hyperelasticity at crack tips. *Nature*, *439*(7074), 307–310. https://doi.org/10.1038/nature04408

Carmichael, J. D., Pettit, E. C., Hoffman, M., Fountain, A., & Hallet, B. (2012). Seismic multiplet response triggered by melt at Blood Falls, Taylor Glacier, Antarctica. *Journal of Geophysical Research: Earth Surface*, *117*(3), 1–16. https://doi.org/10.1029/2011JF002221

Carmichael, J. D., Joughin, I., Behn, M. D., Das, S., King, M. A., Stevens, L., & Lizarralde, D. (2015). Seismicity on the western Greenland Ice Sheet: Surface fracture in the vicinity of active moulins. *Journal of Geophysical Research : Earth Surface*, *120*, 1082–1106. https://doi.org/10.1002/2014JF003398.Received

Colgan, W., Rajaram, H., Abdalati, W., Mccutchan, C., Mottram, R., Moussavi, M. S., & Grigsby, S. (2016). Glacier crevasses: Observations, models, and mass balance implications. *Reviews of Geophysics*, *54*, 119–161. https://doi.org/10.1002/2015RG000504

Das, S. B., Joughin, I., Behn, M. D., Howat, I. M., King, M. A., Lizarralde, D., & Bhatia, M. P. (2008). Fracture propagation to the base of the Greenland Ice Sheet during supraglacial lake drainage. *Science*, *320*, 778–782.

Garcia, L., Luttrell, K., Kilb, D., & Walter, F. (2019). Joint geodetic and seismic analysis of surface crevassing near a seasonal glacier-dammed lake at Gornergletscher, Switzerland. *Annals of Glaciology*, 1–13. https://doi.org/10.1017/aog.2018.32

Gudmundsson, M. T. (1989). The Grimsvotn Caldera, Vatnajokull: Subglacial Topography and Structure of Caldera Infill. *Jokull*, *39*, 3–7.

Hanks, T. C., & Kanamori, H. (1979). A moment magnitude scale. *Journal of Geophysical Research*, *84*(B5), 2348. https://doi.org/10.1029/JB084iB05p02348

Harper, J. T., Humphrey, N. F., & Pfeffer, W. T. (1998). Crevasse patterns and the strain-rate tensor : a high-resolution comparison. *Journal of Glaciology*, *44*(146).

Helmstetter, A., Nicolas, B., Comon, P., & Gay, M. (2015). Basal icequakes recorded beneath an alpine glacier (Glacier d'Argentière, Mont Blanc, France): Evidence for stick-slip motion? *Journal of Geophysical Research: Earth Surface*, *120*(3), 379–401. https://doi.org/10.1002/2014JF003288

Heyburn, R., Selby, N. D., & Fox, B. (2013). Estimating earthquake source depths by combining surface wave amplitude spectra and teleseismic depth phase observations. *Geophysical Journal International*, *194*, 1000–1010. https://doi.org/10.1093/gji/ggt140

Hudson, T S, Brisbourne, A. M., Walter, F., Graff, D., & White, R. S. (n.d.). Icequake source mechanisms for studying glacial sliding. *Journal of Geophysical Research : Earth Surface (in Review)*. https://doi.org/10.1002/essoar.10502610.1

Hudson, Thomas S, Smith, J., Brisbourne, A., & White, R. (2019). Automated detection of basal icequakes and discrimination from surface crevassing. *Annals of Glaciology*, *60*(79), 1–11.

Hughes, B. T. (1983). On the disintegration of ice shelves: The role of fracture. *Journal of Glaciology*, *29*(101), 98–117.

Jia, Z., Ni, S., Chu, R., & Zhan, Z. (2017). Joint inversion for earthquake depths using local waveforms and amplitude spectra of Rayleigh waves. *Pure and Applied Geophysics*, *174*, 261–277. https://doi.org/10.1007/s00024-016-1373-1

Jones, G. A., Kulessa, B., Doyle, S. H., Dow, C. F., & Hubbard, A. (2013). An automated approach to the location of icequakes using seismic waveform amplitudes. *Annals of Glaciology*, *54*(64), 1–9. https://doi.org/10.3189/2013AoG64A074

Krischer, L. (2016). mtspec Python wrappers 0.3.2. *Zenodo*. https://doi.org/10.5281/zenodo.321789

Krug, J., Weiss, J., Gagliardini, O., & Durand, G. (2014). Combining damage and fracture mechanics to model calving. *The Cryosphere*, *8*, 2101–2117. https://doi.org/10.5194/tc-8-2101-2014

Lai, C., Kingslake, J., Wearing, M. G., Chen, P. C., Gentine, P., Li, H., et al. (2020). Vulnerability of Antarctica's ice shelves to meltwater-driven fracture. *Nature*, *584*(7822), 574–578. https://doi.org/10.1038/s41586-020-2627-8

Larsen, S., Wiley, R., Roberts, P., & House, L. (2001). *Next-generation numerical modeling: incorporating elasticity, anisotropy and attenuation*. *Los Alamos National Laboratory* (Vol. LA-UR-01-1).

Lipovsky, B. P., & Dunham, E. M. (2015). Vibrational modes of hydraulic fractures: Inference of fracture geometry from resonant frequencies and attenuation. *Journal of Geophysical Research: Solid Earth*, *120*(2), 1080–1107. https://doi.org/10.1002/2014JB011286

Lomax, A., & Virieux, J. (2000). Probabilistic earthquake location in 3D and layered models. *Advances in Seismic Event Location, Volume 18 of the Series Modern Approaches in Geophysics*, 101–134.

Mcgrath, D., Steffen, K., Scambos, T., Rajaram, H., Casassa, G., Luis, J., & Lagos, R. (2012). Basal crevasses and associated surface crevassing on the Larsen C ice shelf , Antarctica , and their role in ice-shelf instability. *Annals of Glaciology*, *53*(60), 10–18.

https://doi.org/10.3189/2012AoG60A005

Mikesell, T. D., Van Wijk, K., Haney, M. M., Bradford, J. H., Marshall, H. P., & Harper, J. T. (2012). Monitoring glacier surface seismicity in time and space using Rayleigh waves. *Journal of Geophysical Research: Earth Surface*, *117*(2), 1–12. https://doi.org/10.1029/2011JF002259

Neave, K. G., & Savage, J. C. (1970). Icequakes on the Athabasca Glacier. *Journal of Geophysical Research*, *75*(8), 1351–1362.

Nick, F. M., Van Der Veen, C. J., Vieli, A., & Benn, D. I. (2010). A physically based calving model applied to marine outlet glaciers and implications for the glacier dynamics. *Journal of Glaciology*, *56*(199), 781–794.

O'Neel, S., Echelmeyer, K. A., & Motyka, R. J. (2003). Short-term variations in calving of a tidewater glacier: LeConte Glacier, Alaska, U.S.A. *Journal of Glaciology*, *49*(167), 587–598.

Paterson, W. S. B. (1994). *The Physics of Glaciers* (3rd Editio). Oxford: Butterworth-Heinemann.

Podolskiy, E. A., & Walter, F. (2016). Cryoseismology. *Reviews of Geophysics*, *54*, 1–51. https://doi.org/10.1002/2016RG000526

Pollard, D., DeConto, R. M., & Alley, R. B. (2015). Potential Antarctic Ice Sheet retreat driven by hydrofracturing and ice cliff failure. *Earth and Planetary Science Letters*, *412*, 112–121. https://doi.org/10.1016/j.epsl.2014.12.035

Prieto, G. A., Parker, R. L., & Vernon, F. L. (2009). A Fortran 90 library for multitaper spectrum analysis. *Computers and Geosciences*, *35*(8), 1701–1710. https://doi.org/10.1016/j.cageo.2008.06.007

Rignot, E., & Kanagaratnam, P. (2006). Changes in the Velocity Structure of the Greenland Ice Sheet. *Science*, *311*, 986–991. https://doi.org/10.1126/science.1121381

Roux, P. F., Walter, F., Riesen, P., Sugiyama, S., & Funk, M. (2010). Observation of surface seismic activity changes of an Alpine glacier during a glacier dammed lake outburst. *Journal of Geophysical Research*, *115*, 1–13. https://doi.org/10.1029/2009JF001535

Scambos, T., Hulbe, C., & Fahnestock, M. (2003). Climate-induced ice shelf disintegration in the Antarctic Peninsula. *Antarctic Peninsula Climate Variability, Antarctic Research Series*, *79*, 79–92.

Scambos, T. A., Hulbe, C., Fahnestock, M., & Bohlander, J. (2000). The link between climate warming and break-up of ice shelves in the Antarctic Peninsula. *Journal of Glaciology*, *46*(1996).

Smith, J. D., White, R. S., Avouac, J.-P., & Bourne, S. (2020). Probabilistic earthquake locations of induced seismicity in the Groningen region, the Netherlands. *Geophysical Journal International*, *222*(1), 507–516. https://doi.org/10.1093/gji/ggaa179

Stein, S., & Wiens, D. A. (1986). Depth determination for shallow teleseismic earthquakes: Methods and results. *Reviews of Geophysics*, *24*(4), 806–832.

Stork, A. L., Verdon, J. P., & Kendall, J. M. (2014). The robustness of seismic moment and magnitudes estimated using spectral analysis. *Geophysical Prospecting*, *62*(4), 862–878. https://doi.org/10.1111/1365-2478.12134

Tape, W., & Tape, C. (2012). A geometric comparison of source-type plots for moment tensors. *Geophysical Journal International*, *190*(1), 499–510. https://doi.org/10.1111/j.1365-246X.2012.05490.x

Tsai, Y., & Aki, K. (1970). Precise focal depth determination from amplitude spectra of surface waves. *Journal of Geophysical Research*, *75*(29), 5729–5743.

Vaughan, D. ., Comiso, J. C., Allison, I., Carrasco, J., Kaser, G., Kwok, R., et al. (2013). *Chapter 4: Observations: Cryosphere*. *Climate Change 2013 the Physical Science Basis: Working Group I Contribution to the Fifth Assessment Report of the*

Intergovernmental Panel on Climate Change. Cambridge University Press, Cambridge, United Kingdom and New York, NY, USA. https://doi.org/10.1017/CBO9781107415324.012

Van Der Veen, C. J. (1998). Fracture mechanics approach to penetration of surface crevasses on glaciers. *Cold Regions Science and Technology*, *27*(1), 31–47. https://doi.org/10.1016/S0165-232X(97)00022-0

Walter, F., Clinton, J. F., Deichmann, N., Dreger, D. S., Minson, S. E., & Funk, M. (2009). Moment tensor inversions of icequakes on Gornergletscher , Switzerland. *Bulletin of the Seismological Society of America*, *99*(2), 852–870. https://doi.org/10.1785/0120080110

Weertman, J. (1973). Can a water-filled crevasse reach the bottom surface of a glacier. *IASH Publ 95*, 139–145.

Figures

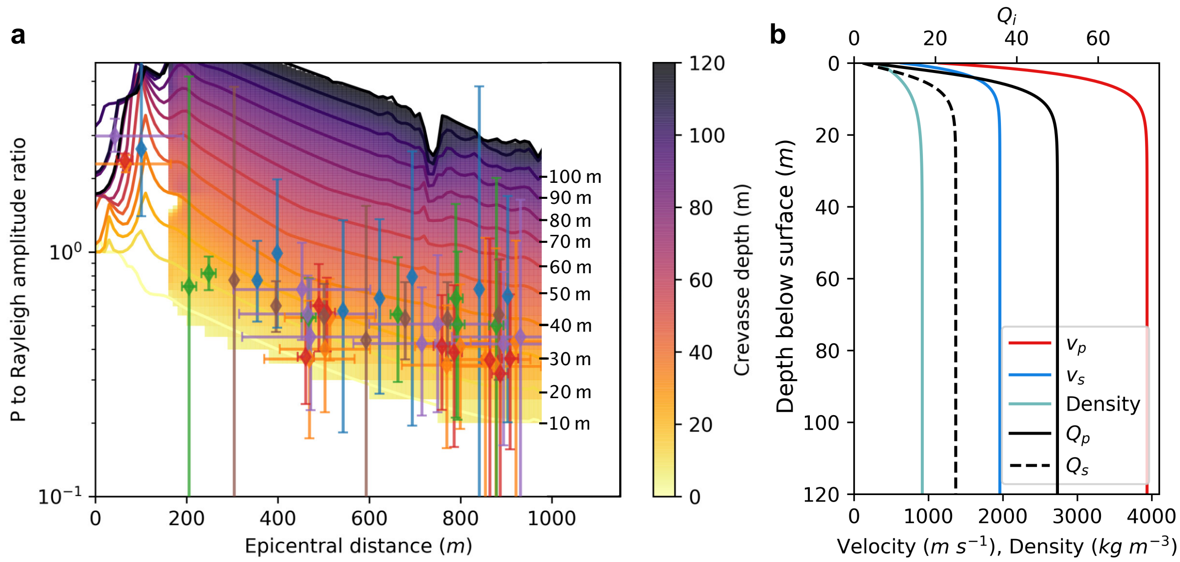

Figure 1 – Obtaining depth for crevassing icequakes. a) Plot of P-to-Rayleigh-wave amplitude ratio with epicentral distance from the source. Observed P-to-Rayleigh amplitudes for the icequakes presented in Figure 2 are plotted (various coloured scatter points). P-to-Rayleigh amplitudes for modelled crevassing icequakes with source depths from 10 to 120 m below surface are indicated by the solid lines, with the 2D interpolated field plotted at epicentral distances greater than 180 m. b) The velocity model used for the modelled crevassing icequakes(Gudmundsson, 1989).

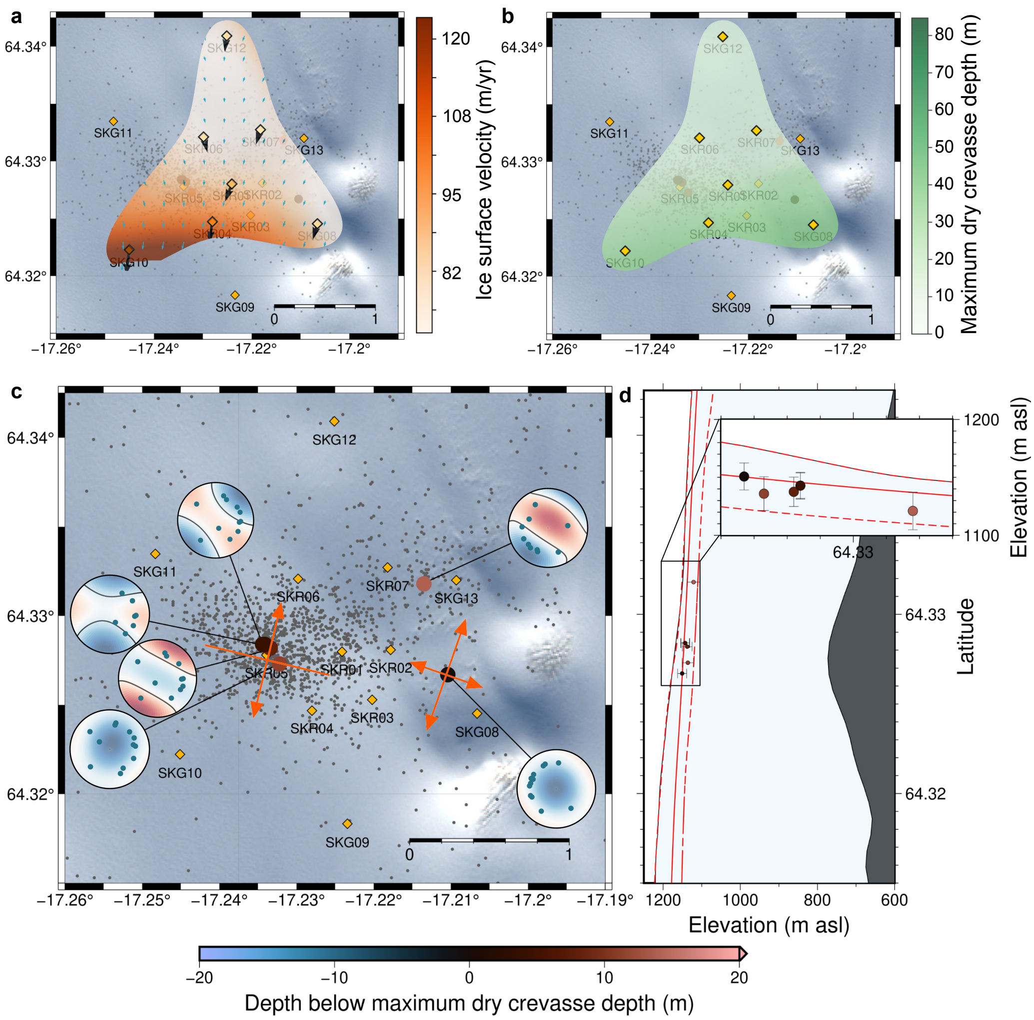

Figure 2 – Summary of crevasse icequake observations. a) The horizontal surface velocity field at the site, derived using GPS data from the highlighted stations. b) The maximum-dry-crevasse-depth, d, calculated using the velocity field in (a). Uncertainty in these fields are given in Figure S2. c) Map of crevasse icequake locations. Grey scatter points are all the crevasse icequakes detected during the period 19th to 29th June 2014. The icequakes studied in more detail, with derived depths using the P-to-Rayleigh amplitude method are plotted as larger scatter points, coloured by depth below the maximum dry crevasse depth. Upper hemisphere moment tensors for these icequakes are also shown. Principal stress vectors derived from the velocity field in (a) are shown in orange. Seismometer and geophone locations are shown by the yellow diamonds. Satellite image is from the European Space*

Agency. d) Plot of the crevassing events in (c) with depth vs. latitude projected onto a N-S transect at 17.225° *W. The solid and dashed red lines indicate the maximum dry crevasse depth and the associated uncertainty, respectively. The bed topography is derived from ground-penetrating radar*(Björnsson, 2017).

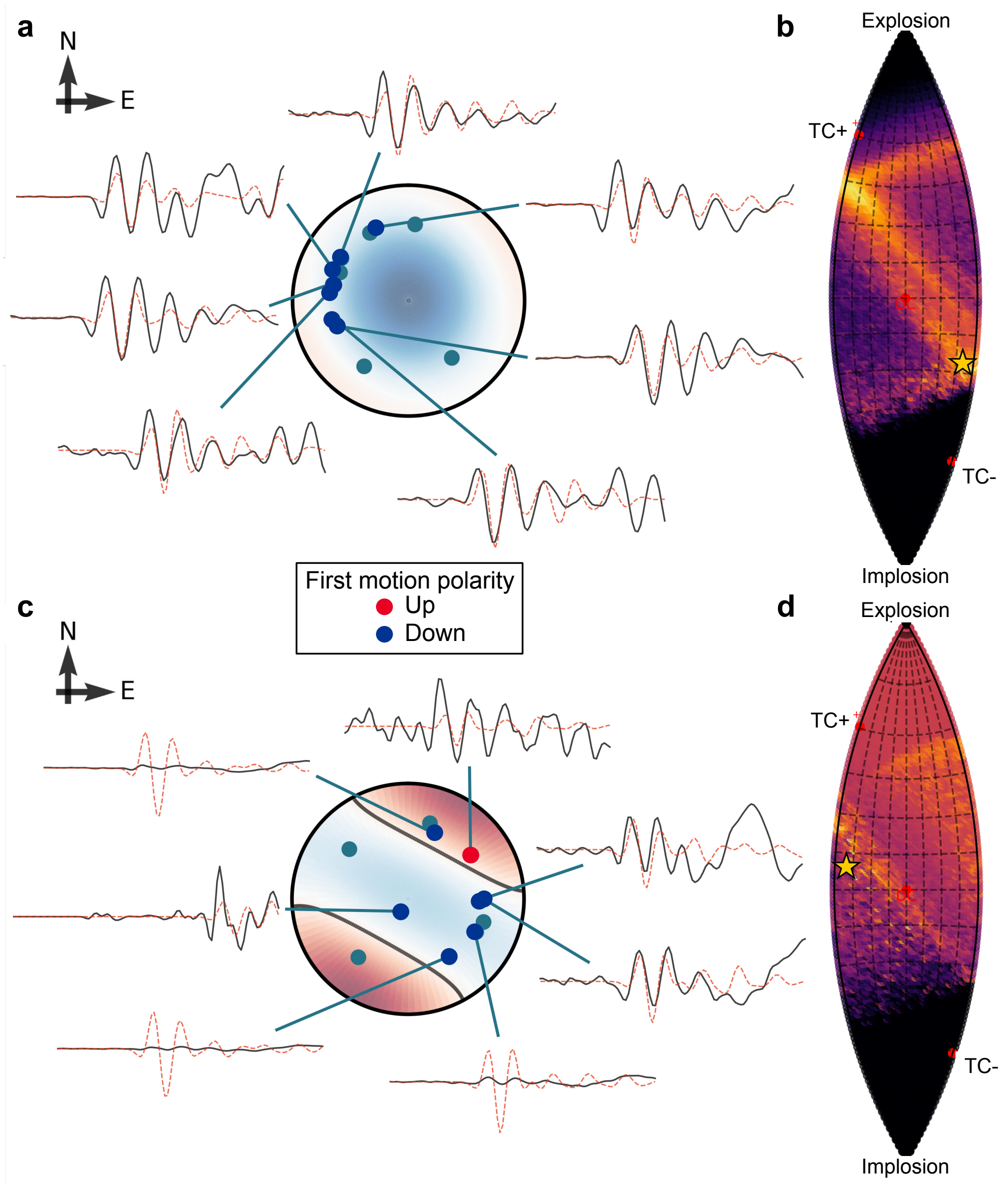

Figure 3 – Examples of upper hemisphere crevasse icequake source mechanisms for two of the events in Figure 2. The source mechanisms are constrained only by P-wave phases. a) Source mechanism for a closing-crack crevasse icequake. Black waveforms are observed data, red dashed waveforms are the most likely inversion model result. b) Lune plot (Tape and Tape (2012)) associated with the event in (a), showing the PDF of the full waveform inversion result, indicating the most likely source type. Brighter colours indicate higher probability. c) and d) Same as (a) and (b) except for an opening-crack crevasse icequake.

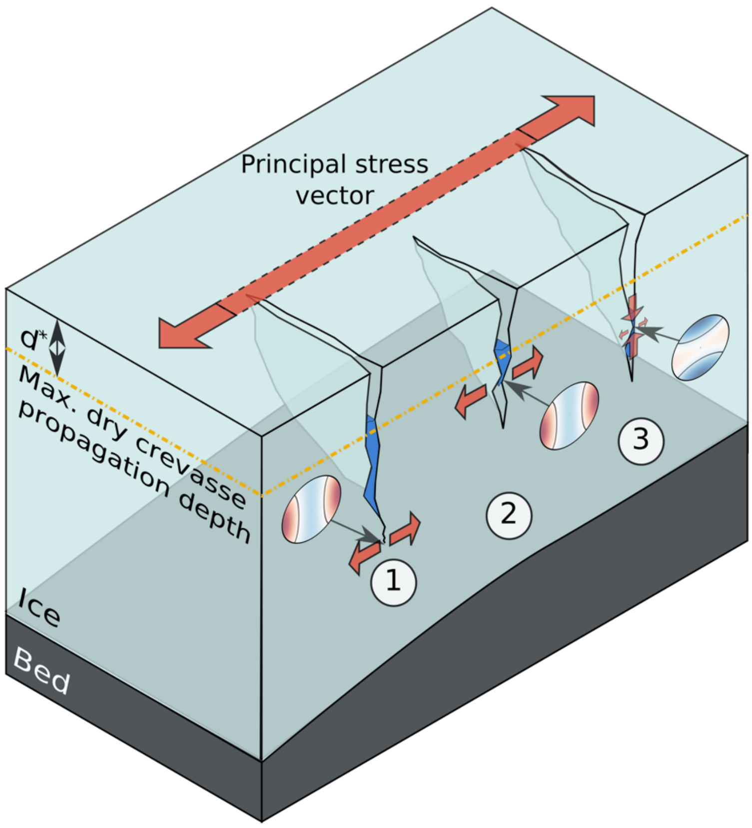

Figure 4 – Interpretation of the possible crevasse failure mechanisms observed. (1) A new opening-crack hydrofracture through previously undamaged ice. (2) An opening-crack hydrofracture of a pre-existing crack. (3) Closing of a pre-existing crack due to the evacuation of water from the crack. Hypothetical source mechanisms are shown for each case.

Supplementary Information for: "Breaking the ice: Identifying hydraulically-forced crevassing"

T.S. Hudson[1*], A.M. Brisbourne[2], R.S. White[3], JM. Kendall[1], R. Arthern[2], A.M. Smith[2]

[1] *Department of Earth Sciences, University of Oxford, Oxford, UK*

[2] *British Antarctic Survey, Cambridge, UK*

[3] *Bullard Laboratories, University of Cambridge, Cambridge, UK*

Corresponding author: Thomas S. Hudson (thomas.hudson@earth.ox.ac.uk)

Supplementary Text S1: P-to-Rayleigh amplitude ratios and icequake depth

The P-to-Rayleigh-wave amplitude ratios are calculated by taking the maximum amplitude within specified windows, as shown for the observed icequake example in Figure S1a. Figure S1c and Figure S1d show the P-to-Rayleigh-wave phase arrivals for one station ~450 m from the source. The particle motion of the inferred Rayleigh-wave is elliptical, providing us with confidence that it is indeed a surface wave arrival. P-wave and Rayleigh-wave windows are of fixed duration for all events, as in Figure S1. The uncertainty in the observed P-to-Rayleigh-wave amplitude ratios is defined as the standard deviation of the noise signal observed in a window 1s prior to the P-phase arrivals. Uncertainty in the epicentral distances given in Figure 1 are defined as the epicentral uncertainty output from NonLinLoc (Lomax & Virieux, 2000). The same method of obtaining P-to-Rayleigh-wave amplitudes is employed for the 2D finite difference modelled seismograms for various source depths from E3D (Larsen et al., 2001). The model is run for various source depths from 10 m to 120 m below surface, with the 2D interpolated field from the model runs (see Figure 2a) used to derive the likely crevasse depth from each receiver observation. These individual receiver observations are then combined for each icequake, to provide an overall estimate of the icequake depth. We independently verify crevasse depth by using S-P delay-times from receivers approximately directly above the crevasse. For the event in Figure S1, the S-P delay-time observed at a receiver approximately above the event is 0.014 s. With the velocity model shown in Figure 1b, this corresponds to an icequake depth of ~25 m below surface, compared to a depth of 29 ± 12 m found using the P-to-Rayleigh amplitude ratios. We are therefore confident that the P-to-Rayleigh-wave amplitude ratios provide a good estimation of icequake depth.

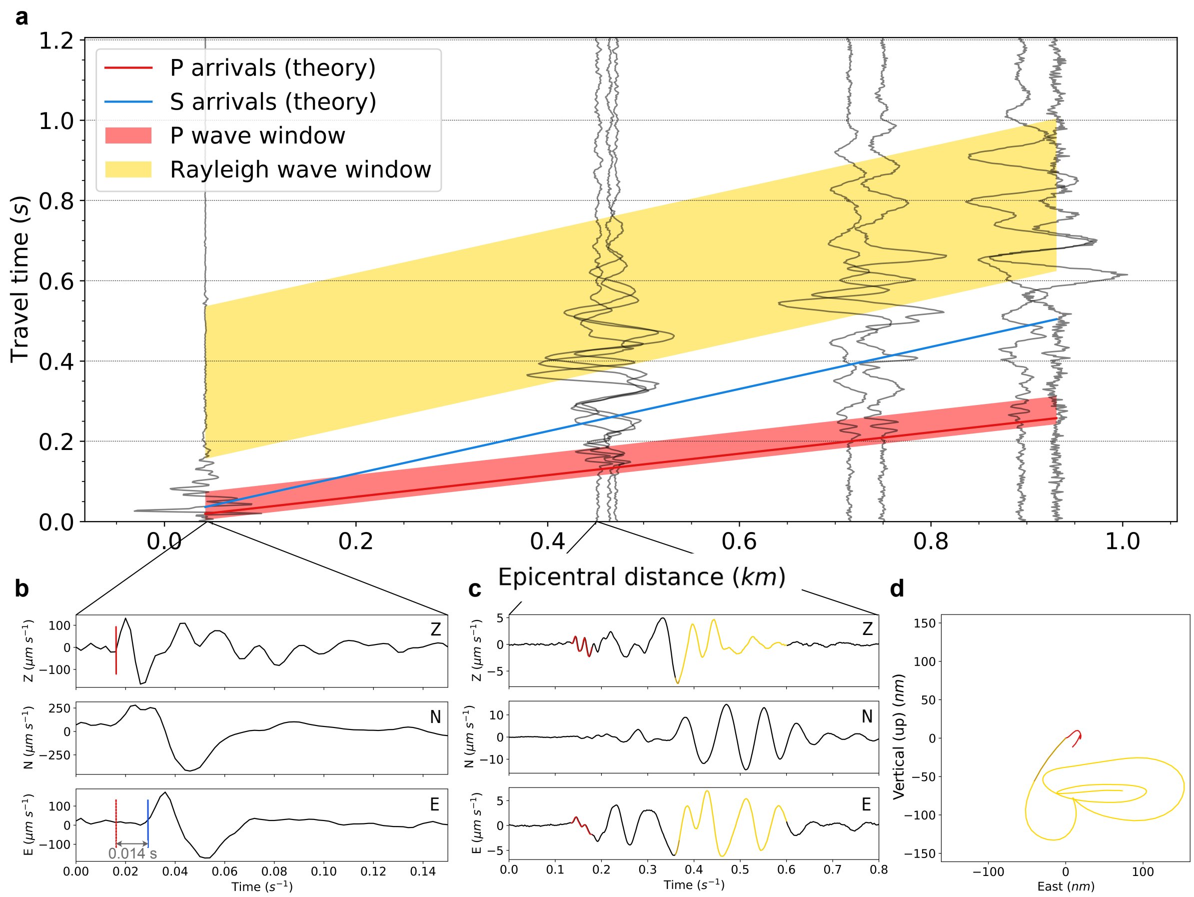

Supplementary Figure S1 – Example of observed waveforms at seismometers from a crevasse icequake at 14:33:52 on 28th June 2014. a) Record section showing the P-to-Rayleigh-wave arrivals. The red and yellow regions show the windows used to calculate the P-to-Rayleigh amplitude ratios. b) Waveforms for an arrival 43 m from the event epicentre. P and S phase arrivals are indicated by the red and blue lines, respectively. c) Waveforms for an arrival 450 m from the event epicentre. d) Particle motions associated with the P and Rayleigh phase arrivals in (c). Red is the P-wave phase and yellow is the Rayleigh wave phase.

Supplementary Text S2: Derivation of maximum-dry-crevasse-depth

The maximum depth to which a crevasse can propagate without hydrofracture is governed by the tensile stress regime near the glacier surface. If the ice is under tensile stress then a crevasse can form. However, as the depth through the ice increases, the ice overburden pressure increases and acts to close the crevasse and prevent further fracture. At a certain depth, the maximum-dry-crevasse-depth, d^*, the maximum principal tensile stress acting to open crevasses becomes equal to the compressive ice overburden pressure. Below this depth, the ice overburden pressure is sufficiently high to prevent opening. This crevassing model is commonly referred to as the zero stress model (Colgan et al., 2016), and has been proven effective in predicting real crevasse depths (Mottram & Benn, 2009).

The above statement assumes that the ice will open under any net tensile stress, which is not strictly correct since the ice also has a tensile failure strength, that we do not account for here. Accounting for the tensile strength of the ice would simply make d^* shallower and hence increase the depth difference between icequake depths and the maximum-dry-crevasse-depth equipotential, therefore increasing the likelihood of icequakes observed being associated with hydrofracture. We also assume that there is a shallow firn layer at the glacier surface, of lower density than the underlying ice. This lower-density layer acts to make the maximum-dry-crevasse-depth deeper. We use the same local seismic refraction survey (Gudmundsson, 1989) as used to constrain the seismic velocities in Figure 1b to constrain the density profile of this layer, making the assumption that the change in velocity in the firn-layer is dominated by density rather than the bulk and shear moduli. This simplified firn density correction is assumed adequate for the purposes of this study since the weight estimation of the firn layer is conservative, therefore resulting in an overestimate of the maximum-dry-crevasse-depth.

To find d^*, one has to calculate the stress field near the glacier surface. This can be approximately obtained using the glacier surface velocity field. For a given point on the glacier, the velocity is defined by,

$$\overrightarrow{v_{i,j}} = \begin{pmatrix} u_{i,j} \\ v_{i,j} \\ w_{i,j} \end{pmatrix}, \qquad (3)$$

where u, v and w are the velocities in the x, y and z directions, and i, j denotes a particular horizontal location within the velocity field. To obtain the velocity field for the glacier surface at Skeidararjökull, we use GPS location data from the seismometers shown in Figure 2. The GPS data from the seismometers is more poorly constrained compared to dedicated dual-frequency GPS instruments, and is sampled only once per hour. Therefore, in order to reduce the GPS noise, we use a seven day moving average for the latitude, longitude and elevation data. We then calculate the average velocity over the ten day period of analysis. Even after applying this processing, data from only 7 stations are of sufficient quality to use. We then perform a two-dimensional, second-order interpolation for these velocity data points in order to obtain a horizontal velocity field for the network area. Due to only one station, SKR12, constraining the velocity field for the upper half of the network area, the interpolation scheme performs poorly outside the network, so we only analyse the velocity field approximately within the network, as shown in Figure 2 and Figure S2.

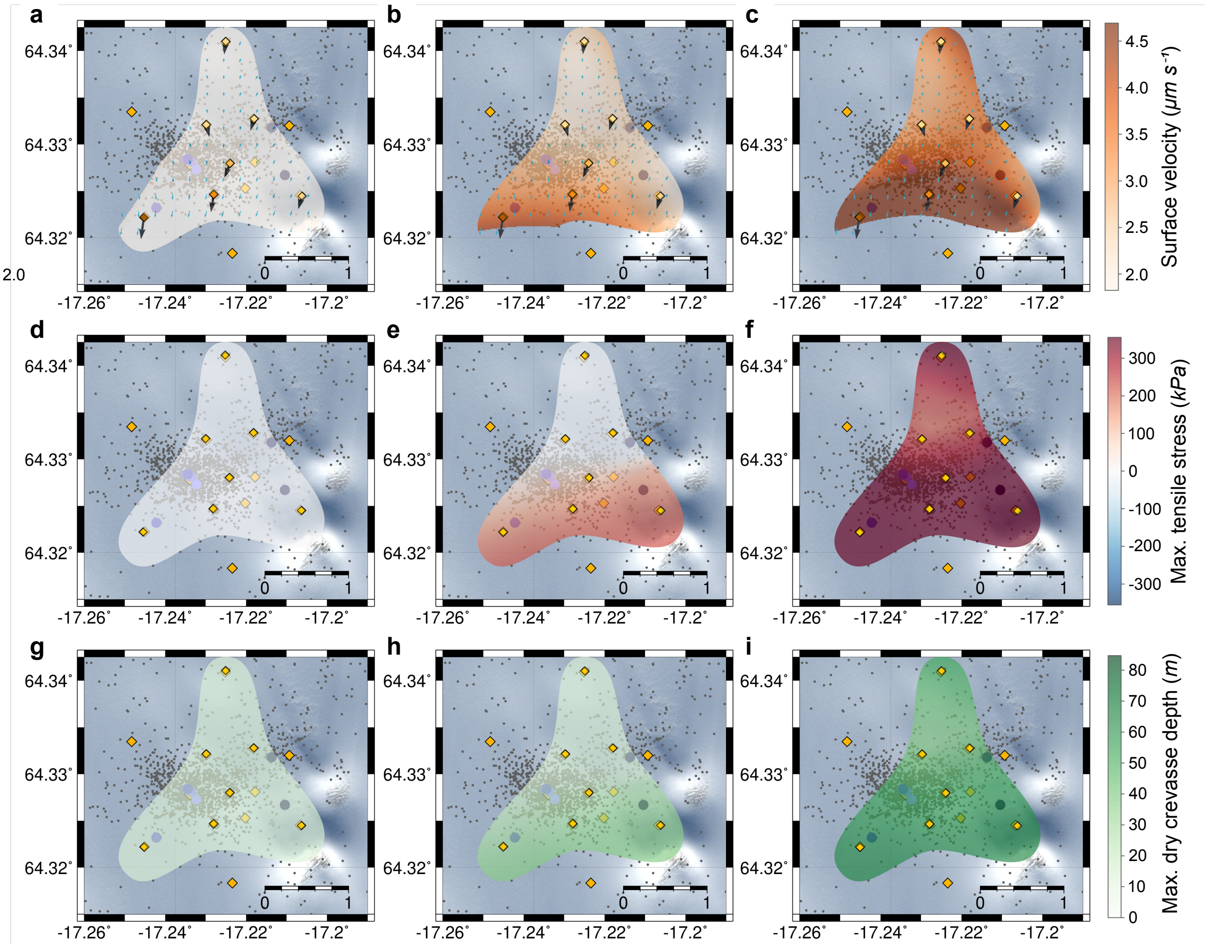

Figure S2 - The estimated uncertainty in the interpolated maximum surface velocity, maximum principal tensile stress and maximum-dry-crevasse-depth fields. (a) to (c) The lower, actual and upper uncertainty associated with the surface velocity field, respectively. (d) to (f) The lower, actual and upper uncertainty associated with the maximum principal stress field, respectively. (g) to (i) The lower, actual and upper uncertainty associated with the maximum-dry-crevasse-depth, respectively.

The velocity field can then be used to obtain the strain rate field for each point on the glacier surface. The second order strain rate tensor is given by,

$$\dot{\boldsymbol{\varepsilon}} = \begin{pmatrix} \dot{\varepsilon}_{xx} & \dot{\varepsilon}_{xy} & \dot{\varepsilon}_{xz} \\ \dot{\varepsilon}_{xy} & \dot{\varepsilon}_{yy} & \dot{\varepsilon}_{yz} \\ \dot{\varepsilon}_{xz} & \dot{\varepsilon}_{yz} & \dot{\varepsilon}_{zz} \end{pmatrix} = \begin{pmatrix} \frac{\partial u}{\partial x} & \frac{1}{2}\left(\frac{\partial u}{\partial y} + \frac{\partial v}{\partial x}\right) & 0 \\ \frac{1}{2}\left(\frac{\partial u}{\partial y} + \frac{\partial v}{\partial x}\right) & \frac{\partial v}{\partial y} & 0 \\ 0 & 0 & \frac{\partial w}{\partial z} \end{pmatrix}. \quad (4)$$

$\dot{\varepsilon}_{xz}$ and $\dot{\varepsilon}_{yz}$are taken to be zero, assuming no shear with depth, a realistic approximation near the glacier surface. If one also assumes that ice is incompressible, then $tr(\dot{\boldsymbol{\varepsilon}}) = 0$. $\dot{\varepsilon}_{zz}$ can then be found, giving,

$$\dot{\varepsilon}_{zz} = \frac{\partial w}{\partial z} = -\left(\frac{\partial u}{\partial x} + \frac{\partial v}{\partial y}\right). \quad (5)$$

To find the maximum-dry-crevasse-depth, we require the stress tensor. In order to calculate the stress tensor from the strain tensor, we need one final piece of information, the effective viscosity, η_{eff}, for a given horizontal location. Since ice behaves as a non-linear fluid, η_{eff} varies with the strain rate, $\dot{\boldsymbol{\varepsilon}}$. The effective viscosity is defined as,

$$\boldsymbol{\eta_{eff}} = \frac{B}{2}\left(\dot{\boldsymbol{\varepsilon}}_{\boldsymbol{eff}}\right)^{\frac{1}{n}-1}, \quad (6)$$

where B is given by,

$$B = A^{-\frac{1}{n}}, \quad (7)$$

where the temperature-dependent rate factor $A = 5.6 \times 10^{-17}\ Pa^{-3}\ a^{-1}$ and $n = 3$, determined from laboratory studies (Glen, 1955; Nick et al., 2010). The effective strain rate, $\dot{\boldsymbol{\varepsilon}}_{\boldsymbol{eff}}$, is defined by,

$$\dot{\boldsymbol{\varepsilon}}_{\boldsymbol{eff}} = |\dot{\boldsymbol{\varepsilon}}| = \left(\frac{1}{2}\ tr(\dot{\boldsymbol{\varepsilon}} \,.\, \dot{\boldsymbol{\varepsilon}})\right)^{\frac{1}{2}}. \quad (8)$$

The net stress tensor, $\boldsymbol{\sigma}$, is then defined as the difference between the opening stress and the ice overburden stress tensor by,

$$\boldsymbol{\sigma} = \boldsymbol{\sigma_{opening}} - \boldsymbol{\sigma_{overburden}}\,, \quad (9)$$

which can be written explicitly as,

$$\boldsymbol{\sigma} = \begin{pmatrix} 4\eta_{eff}\varepsilon_{xx,i,j} + 2\eta_{eff}\varepsilon_{yy} & 2\eta_{eff}\varepsilon_{xy} & 0 \\ 2\eta_{eff}\varepsilon_{xy} & 4\eta_{eff}\varepsilon_{yy} + 2\eta_{eff}\varepsilon_{xx} & 0 \\ 0 & 0 & 0 \end{pmatrix} - \rho g z \boldsymbol{I}\,, \quad (10)$$

where ρ is the ice density, g is the gravitational constant of acceleration and z is the depth below the ice surface. $\sigma_{opening,xz}$ and $\sigma_{opening,yz}$ are zero since we have assumed no vertical shear stress with depth and $\sigma_{opening,zz}$ is zero, assuming that the ice is in hydrostatic equilibrium. At the maximum-dry-crevasse-depth is where the maximum principal opening stress equals the overburden stress, at which point z is the maximum-dry-crevasse-depth, d^*. Therefore, to find d^* we need to find the maximum principal opening stress, $\boldsymbol{\sigma^*_{opening}}$. To do this, we rotate $\boldsymbol{\sigma}$ to maximise the tensile stress,

$$\boldsymbol{\sigma^*_{opening}} = \boldsymbol{S}\,\boldsymbol{\sigma_{opening}}\,\boldsymbol{S^T}, \quad (11)$$

where **S** is a rotation matrix comprising the eigenvectors of $\boldsymbol{\sigma_{opening}}$. The maximum-dry-crevasse-depth at a given point on the glacier surface, d^*, is then given by (Nick et al., 2010),

$$d^* = \frac{max\left(\boldsymbol{\sigma^*_{opening}}\right)}{\rho g}. \quad (12)$$

The uncertainty associated with the maximum-dry-crevasse-depth field is proportional to the uncertainty in the velocity field. To estimate the uncertainty, we calculate the standard deviation in the average velocity data and randomly perturb the velocity data used to calculate the velocity field by gaussian distributions about the average observed velocities, with the standard deviations used to constrain the width of these distributions. These gaussian distributions are sampled 1000 times. We then calculate the strain, stress, and crevasse depth fields from each perturbed velocity field, and define the lower and upper uncertainties for each field as the minimum and maximum values, respectively, for each point spatially within the fields. This data is shown by the red dashed lines in Figure 2d, and all the fields and their associated uncertainties are shown in Figure S2.

Supplementary references (also cited in main text)

Colgan, W., Rajaram, H., Abdalati, W., Mccutchan, C., Mottram, R., Moussavi, M. S., & Grigsby, S. (2016). Glacier crevasses: Observations, models, and mass balance implications. *Reviews of Geophysics*, *54*, 119–161. https://doi.org/10.1002/2015RG000504

Glen, J. W. (1955). The creep of polycrystalline ice. *Proceedings of the Royal Society of London. Series A, Mathematical and Physical Sciences*, *228*(1175), 519–538. https://doi.org/10.1098/rspa.1955.0066

Gudmundsson, M. T. (1989). The Grimsvotn Caldera, Vatnajokull: Subglacial Topography and Structure of Caldera Infill. *Jokull*, *39*, 3–7.

Mottram, R. H., & Benn, D. I. (2009). Testing crevasse-depth models: a field study at Breiðamerkurjokull, Iceland. *Journal of Glaciology*, *55*(192), 746–752.

Nick, F. M., Van Der Veen, C. J., Vieli, A., & Benn, D. I. (2010). A physically based calving model applied to marine outlet glaciers and implications for the glacier dynamics. *Journal of Glaciology*, *56*(199), 781–794.